Effectiveness of photocatalysis of MMT-supported TiO2 and TiO2 nanotubes for rhodamine B degradation

Thi Bang Tam Dao, Thi Thu Loan Ha, Trung Do Nguyen, Hon Nhien Le, Chi Nhan Ha-Thuc, Thi Mai Loan Nguyen, Patrick Perré, Dang Mao Nguyen

Effectiveness of photocatalysis of Montmorillonite-supported TiO_2 and TiO_2 nanotubes for rhodamine B degradation

Thi Bang Tam Dao[a,b], Thi Thu Loan Ha[a,b], Trung Do Nguyen[a,b], Hon Nhien Le[a,b], Chi Nhan Ha-Thuc[a,b*], Thi Mai Loan Nguyen[c], Patrick Perre[d*], Dang Mao Nguyen[d*]

[a]Faculty of Materials Science and Technology, University of Science, VNU-HCM, 227 Nguyen Van Cu Street, Ward 4, District 5, Ho Chi Minh City, 700000, Viet Nam

[b]Vietnam National University – Ho Chi Minh City, Linh Trung Ward, Thu Duc District, Ho Chi Minh City, 700000, Viet Nam

[c]Institute of Research and Development, Duy Tan University, Da Nang 550000, Viet Nam.

[d]Université Paris-Saclay, CentraleSupélec, Laboratoire de Génie des Procédés et Matériaux, SFR Condorcet FR CNRS 3417, Centre Européen de Biotechnologie et de Bioéconomie (CEBB), 3 rue des Rouges Terres 51110 Pomacle, France

* Corresponding authors: htcnhan@hcmus.edu.vn (C.N. Ha-Thuc); patrick.perre@centralesupelec.fr (P. Perré); dang-mao.nguyen@centralesupelec.fr (D.M. Nguyen).

ABSTRACT

The aim of this paper is to synthesize montmorillonite/TiO_2-nanoparticles (MMT/TiO_2 and montmorillonite/TiO_2-nanotubes (MMT/$TiO_{2\text{-NTs}}$) photocatalysts through a simple wet agitation method based on TiO_2 nanoparticles and MMT. They are likely to accumulate the effect of adsorption and photodegradation. Then, the photocatalysts are

applied to degrade the rhodamine B in dye effluents. The structural characterizations of photocatalysts are investigated using transmission electron microscopy (TEM), scanning electron microscopy (SEM), X-ray diffraction (XRD), Fourier transform infrared spectroscopy (FTIR) and energy-dispersive X-ray spectroscopy (EDX). The photocatalytic activities and effectiveness of photocatalysts are evaluated through rhodamine B degradation at different concentrations under dark and UV-C irradiation conditions. The results show that the synthesized $TiO_{2\text{-}NTs}$ have an average tube diameter of 5 nm and a tube length at least about 110 nm, which are intercalated into MMT sheets in MMT/$TiO_{2\text{-}NTs}$ photocatalyst. Meanwhile, TiO_2 nanoparticles are immobilized on the surface of MMT sheets in the MMT/TiO_2 photocatalyst. The photocatalytic effectiveness of rhodamine B degradation of $TiO_{2\text{-}NTs}$ shows a significantly enhance compared to that of TiO_2 nanoparticles. However, photocatalytic performance of MMT/$TiO_{2\text{-}NTs}$ is lower than that of MMT/TiO_2. The degradation effectiveness of MMT/TiO_2 photocatalyst reaches to 100% for 3ppm and 90% at 10ppm of rhodamine B, while these values are 97.5% and 85.5%, respectively, recorded for MMT/$TiO_{2\text{-}NTs}$.

Keywords: *Photocatalysts, UV-C irradiation, TiO_2 nanotubes, MMT/*TiO_2 and MMT/$TiO_{2\text{-}NTs}$, and rhodamine B.

1. Introduction

Synthetic dyes are widely used in various applications in the industries as paper, leather, and textile due to their color-giving properties (Gupta and Suhas, 2009; Abdi et al., 2017; Katheresan et al., 2018; Wang et al., 2020). They are responsible for environmental

pollutions and human health (Charumathi and Das, 2012) due to the presence of dye in effluents. It was stated that some of the following industries are mainly responsible for environmental pollution from dye effluent such the textile (54%), the dyeing industry (21%), paper and pulp (10%), tannery and paint (8%) and the dye manufacturing (7%) (Rauf and Salman Ashraf, 2012) and other activities as dyes degradation (dos Santos et al., 2007). Rhodamine B is a xanthene dye, which is widely used as a colorant in textiles industry, wool, silk, dye cells in biotechnology and food stuffs. However, it is harmful to human and animal as skin, eyes and respiratory tract irritation, carcinogenicity as well as reproductive and developmental toxicity (Kingsley et al., 1990; Nagaraja et al., 2012). Therefore, the removal of rhodamine B from dyes effluents must be given priority before they are released into environment. Until now, there was some methodologies of removing of the dyes from wastewaters including chemical, physical methods and biological processes, however, they still have many disadvantages such as low efficiency and high cost (Robinson et al., 2001). Photocatalyst approaches are currently being investigated for the removal of impurities in wastewater. Photocatalytic is a new and potential discovery that uses renewable energy sunlight to decompose organic pollutants into low-cost but highly efficient fuels and removal of trace contaminant from water (Malato et al., 2009). This approach is also environmentally friendly, compared to previous traditional methods such as advanced oxidation, filters, and solar evaporation. In recent years, the use of semiconductor photocatalytic materials for treatment of organic compounds has achieved remarkable achievements and attracted from basic research to application. Some of them have been studied and used as photocatalysts such as ZnO,

67 CdS, and Fe_2O_3 (Hassani et al., 2017; Pannak et al., 2018). Titanium dioxide (TiO_2) is
68 known as a potential photocatalyst in the field of environmental cleaning because of its
69 chemical and biological inertness, ease of fabrication, non-toxicity, abundance in
70 availability and low cost (Hassani et al., 2017; Chinh et al., 2018; Chinh et al., 2019). In
71 particular, TiO_2 has been widely studied for photocatalysis (Fan et al., 2014; Huang et al.,
72 2016; Tahir and Amin, 2016). However, TiO_2 has limitations in photocatalytic
73 applications due to the rapid recombination between electron and holes pairs, which
74 cause to reduce photocatalytic efficiency. Moreover, it also has a wide band gap that only
75 active photocatalyst in the ultraviolet light (less than 5% of the entire solar energy),
76 inducing a lower photocatalytic activity (Leong et al., 2014; Diamond et al., 2017). To
77 overcome the above limitations, some approaches are proposed to improve the
78 photocatalytic activity. Specifically, TiO_2 nanosheets were used as an electron mediator
79 to prepare the CdSe/graphene/TiO_2 nanosheet composite photocatalysts. They provided a
80 great efficient charge separation, extended visible-light absorption range and stability for
81 the degradation of methylene blue in aqueous solutions (Ma et al., 2018). Moreover, the
82 TiO_2 nanosheets were combined with small plasmonic Au nanoparticles to improve the
83 photocatalytic rate of hydrogen production through the large surface adsorptive sites for
84 reactant adsorption and enhancing the charge separation through the Schottky transfer
85 hub to neighboring TiO_2 nanosheets (Cheng et al., 2019). It could be combined with
86 different semiconducting materials (Zhang et al., 2020) to prevent reuniting the
87 photogenerated electron-hole pairs (Dao et al., 2020) and improve the photocatalytic
88 activities (Low et al., 2018). $TiO_{2\text{-}NTs}$ are synthesized through hydrothermal method from

TiO_2. They can improve the photocatalytic activity due to large specific surface area, ion exchange capacity, and fast electronic transfer over a long distance, and high adsorption of light due to a large ratio between the length and diameter of the tubes. Specially, all these properties could be obtained and controlled through the synthesis method (Casu et al., 2018; Niu et al., 2020). Unfortunately, similar to most semiconductor materials used as photocatalyst, $TiO_{2\text{-}TNs}$ are also difficult in separating the electron–hole pairs, leading to reduce photocatalytic activity. Therefore, some strategies have been proposed to extend the lifetime of photoinduced charge carriers and enhance photocatalytic activities including doping metal (Park et al., 2011; Sasani et al., 2016), metal oxides (Xu et al., 2014; Habila et al., 2016) and non-metals such as Zeolite, and Carbon and Montmorillonite (MMT) (Yin et al., 2014; Hassani et al., 2016). MMT is purified from bentonite and available in large reserves from natural mineral sources (Thuc et al., 2010). Specially, it combines a low cost with interesting properties due to its layered structure, large surface area, cation exchange ability and high heat resistance. It is considered as potential material to be combined with TiO_2 and $TiO_{2\text{-}NTs}$ to create novel materials, which could be used to degrade and store pollutants and toxic agents in wastewater (Hassani et al., 2017; Szczepanik, 2017a; Shan et al., 2020). In the literature, a study has successfully synthesized MMT/TiO_2 from Tetraethyl orthotitanate for Ciprofloxacin (CIP) treatment. The results showed that the CIP degradable efficiency of MMT/TiO_2 nanocomposites reached up to 65.01% after 120 min adsorption time, which was much higher than that of MMT or TiO_2 only (Hassani et al., 2017). The photocatalytic effect of TiO_2/MMT doping with Y^{3+} (Yttrium) into TiO_2 for Methyl Orange (MO) treatment was reported (Bing et

al., 2015). Thus, Y^{3+} reduces the band gap to increase the photocatalytic capacity of TiO_2, leading to increase the efficiency of MO degradation. In addition, MMT/TiO_2 nanocomposite was produced by hydrothermal method to obtain the TiO_2 particles range about 40-60 nm to treat Basic Blue 3 (BB3) (Khataee et al., 2015). The results showed that the photocatalytic performance of MMT/TiO_2 was much higher than that of MMT and TiO_2 under different pH and BB3 concentration. In addition, it was reported that rhodamine B was degraded by various photocatalysts, which was clearly described in previous literature (Natarajan et al., 2011; Shi et al., 2014; Wang et al., 2020). The degradation process could be explained by the fact that the active radicals such as hydroxyl free radicals (•OH), and free superoxide radicals ($\bullet O_2^-$), attack the central carbon in the rhodamine B molecules and oxidize them to low-weight intermediates. In the opening-ring process, the active radicals attack the simple intermediates that are produced, which results in the formation of small and broken-ring compounds. The smaller compounds are degraded to CO_2 and H_2O.

In this paper, we will synthesis of MMT/TiO_2 and MMT/$TiO_{2\text{-NTs}}$ photocatalysts with a low-cost hydrothermal method. These combinations could maximize the photocatalytic capabilities under dark and UV-C irradiation conditions for rhodamine B degradation at different concentrations from dyeing wastewater compared to TiO_2 and $TiO_{2\text{-TNs}}$ only, because they are likely to slowdown of electron and holes pairs recombination. Moreover, the reusability of MMT/TiO_2 and MMT/$TiO_{2\text{-NTs}}$ for the rhodamine B degradation was repeated three time under the same conditions to evaluate the stability of the photocatalytic activities.

2. Materials and experiment

2.1. Materials

Rhodamine B was purchased from Sigma-Aldrich in highest purity. Montmorillonite (purity > 95%) was purified from bentonite in Lam Dong Province, Vietnam. Acid nitric, Sodium hydroxide, Ethanol, Sodium Chloride were purchased from Merck (Germany).

2.2. MMT preparation

200 g Bentonite and 5L distilled water were stirred for 24 hours and settled for 5 hours. 1 g of NaCl was added and mechanical stirred for 3 hours and settled for 24 hours. The suspension obtained was centrifuged for 30 min with a speed of 3500 rpm. The collected solids were washed with distilled water for 4 hours and settled for 8 hours. Ethanol (30%) was added to the above solution and stirred for 30 min before being settled for 24 hours. Then, the suspension was centrifuged for 30 min at 3500 rpm to obtain high purity MMT. Finally, MMT was dried at 60 °C for 72 hours. The purification of MMT from Bentonite could be referenced in previous studies (Thuc et al., 2010; Nguyen Van et al., 2020).

2.3. Preparation of $TiO_{2\text{-}NTs}$

$TiO_{2\text{-}NTs}$ were synthesized by hydrothermal method from TiO_2 powder with particle size in the range of 50-60 nm. 4.2 g of TiO_2 powder was added slowly into 10M NaOH solution with TiO_2/NaOH molar ratio of 1/30 and stirred for 4 hours at 50°C. The suspension solution obtained was poured into a Teflon flask, which was then inserted into a stainless-steel jar and sealed. Hydrothermal process was then performed at 130°C for 24

hours in an autoclave before cooling to the room temperature. The product after hydrothermal process was filtered and washed with deionized water to reach a pH = 9. The solid product was then dispersed in deionized water and adjusted to pH = 7 with 2M HNO_3 solution and stirring for 2 hours before centrifuging to obtain solid product. Once again, the product was dispersed into deionized water at 80°C and stirred to remove the salt formed during the above reaction. The solid product was then obtained by centrifugation for 15 min and dried at 60°C for 24 hours. Finally, the product was heated at 400°C with a heating rate of 5 °/min and maintained at the final temperature for 2 hours to obtain $TiO_{2\text{-}TNs}$ (Wong et al., 2011; Farghali et al., 2014).

2.4. Preparation of MMT/TiO_2 and MMT/$TiO_{2\text{-}TNs}$ photocatalysts

2.00 g of MMT was slowly added to 100 mL of deionized water and mechanical stirred 500rpm for 24 hours to allow MMT to expand completely. Then, 0.206 g TiO_2 was added slowly to the above MMT suspension and stirred 500 rpm for 4 hours. This suspension solution was then treated by ultrasound (UPH100) at 100 W and frequency 30 kHz for 1 hour . The product was obtained through centrifugation process with a rotating speed of 3500 rpm for 15 min. Finally, the product was dried at 80°C in an oven for 24 hours to obtain MMT/TiO_2 photocatalyst. MMT/$TiO_{2\text{-}NTs}$ photocatalyst was synthesized with similarly process and proportion for MMT/TiO_2 photocatalysts. The contents of MMT/$TiO_{2\text{-}NTs}$ and MMT/TiO_2 were calculated based on the cation exchange capacity of montmorillonite clay (CEC_{MMT} = 86 mmol/100g).

2.5. Photocatalysts characterizations

The characteristic vibration of functional groups in photocatalysts was characterized using a Fourier transform infrared (FT-IR) spectrometer Nicolet iS 50 (FT-IR, Thermo, USA) in the range 4000 to 400 cm^{-1} with a resolution of 2 cm^{-1}. The structure of TiO_2, $TiO_{2\text{-}NTs}$, MMT and nanocomposites was evaluated by X-ray diffraction using D2-PHASER diffractometer (Bruker, Germany) with a Ni-filtered CuK radiation (λ=1.54 Å) at 40 kV, 40 mA, scan rate 0.030 º/sec, and scan angle 2θ = 5-80º. The SEM technique was used to evaluate the surface morphology of materials using a S4800 (Hitachi co., Japan). Samples were fixed on an aluminum stub for scanning electronic microscope using a carbon double-side tape. The following conditions were applied to obtain the images: secondary electron detector, high vacuum mode, an accelerating voltage of 10 kV, a spot size of 3 and a work distance of approximate 9 mm. The non-conductive samples were first coated with gold before being scanned. Finally, the structure of $TiO_{2\text{-}NTs}$ and the state of $TiO_{2\text{-}TNs}$ intercalation into MMT sheets in MMT/$TiO_{2\text{-}TNs}$ photocatalyst are observed by JEM-1400 Transmission Electron Microscope (TEM) equipment (JEOL, Japan) with an acceleration voltage 120kV. Energy-dispersive X-ray (EDX) spectroscopy (HORIBA H-7593) was used to detect and quantify the metallic elemental compositions in materials. The X-ray peak intensity is proportional to the percentage of elements present in the test sample.

2.6. Evaluation of the photocatalytic activity of materials

The adsorption ability and degradation of rhodamine B from dyeing wastewater of nanocomposites was evaluated in dark condition and irradiation condition by UV-C lamp, respectively. In the dark condition, 10 mg of each photocatalyst was slowly added to 100 mL of rhodamine B solution at an initial concentration of 10 ppm (C_o) and stirred for 60 min. Then, every 30 min, 5 mL of the solution was extracted and centrifuged at 3500 rpm for 15 min to separate the material from the dye solution. The portion of the obtained solution was used to measure UV –Vis and calculate the decomposition efficiency.

For experiment with UV-C irradiation, a light source at a wavelength of 254 nm with 15W was used. Similar to the dark condition, 10 mg of test materials were added to 100 mL of rhodamine B solution. The solution was first stirred in the dark condition for 60 min. Then, UV-C lamp (UVC 16W - Philip) was used to light the solution. Every 30 min, 5 ml of solution was extracted and centrifuged at 3500 rpm for 15 min to eliminate the solid to remove the solid. The obtained solutions in dark and UV-C irradiation conditions were then measured with UV–Vis spectrometer (Jasco V-670) with a range of 400 to 700 nm, step size of 0.5 nm, and scanning speed of 400 nm/min.

3. Results and discussion

3.1. SEM and TEM images analysis of photocatalysts

The mechanism of $TiO_{2\text{-}NTs}$ formation is assumed that under hydrothermal condition, the Ti-O-Na and Ti-OH bonds are gradually formed under the influence of high concentrated NaOH solution. Then, the high surface energies of Ti-O-Na and Ti-OH lead to the coiling

221 and formation of $TiO_{2\text{-}TNs}$. The Ti-O-Ti bonds are created after water removal and heated
222 for 2 hours at 400°C (Cui et al., 2012). TEM image of $TiO_{2\text{-}NTs}$ is presented in Figure 1a.
223 The $TiO_{2\text{-}TNs}$ are formed from different directions with relatively uniform size as an
224 average tube diameter of about 5 nm and tube length at least about 110 nm. The SEM
225 analysis of pure MMT, MMT/TiO_2 and MMT/$TiO_{2\text{-}NTs}$ photocatalysts is displayed in
226 Figure 1 (b-d), respectively. As showed in Figure 1b, the MMT is stacked by sheets with
227 different sizes and shapes. Figure 1c clearly displays the morphology of MMT
228 immobilized TiO_2 particles. The TiO_2 particles are evenly dispersed on the surface of
229 MMT sheets with nanosized range from 30 to 45 nm. This result is suitable with previous
230 observations (Yin et al., 2014; Shiding Miao et al., 2016; Mishra et al., 2017). However,
231 the dispersion and morphology of MMT/$TiO_{2\text{-}NTs}$ is much differential to MMT/TiO_2,
232 where $TiO_{2\text{-}NTs}$ are intercalated and dispersed randomly between MMT sheets to produce
233 heterogeneous structure. The nanotubes morphology can be observed as presented in
234 Figure 1d. In addition, the clearly structure and morphology of MMT/$TiO_{2\text{-}NTs}$
235 photocatalyst is described through the TEM analysis in Figure 2.

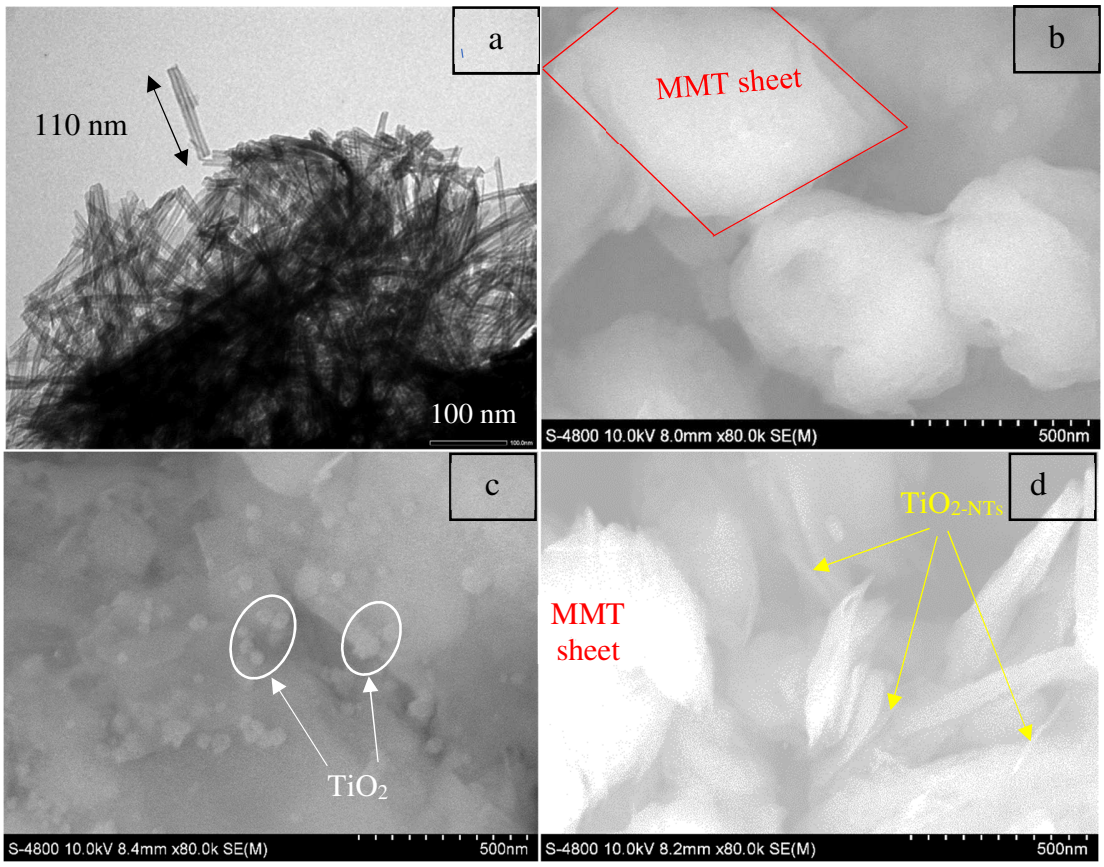

Figure 1. The TEM image of $TiO_{2\text{-}NTs}$ structure synthesized through hydrothermal method (a); and the SEM analysis of pure MMT (b), MMT/TiO_2 (c) and (d) MMT/$TiO_{2\text{-}NTs}$.

This Figure highlights that $TiO_{2\text{-}NTs}$ and MMT sheets are intercalated in MMT/$TiO_{2\text{-}NTs}$ photocatalyst compared to MMT sheets immobilized TiO_2 particles in the MMT/TiO_2 photocatalyst. The MMT sheets are presented as the red-edged black blocks are surrounded by $TiO_{2\text{-}NTs}$. Moreover, the TEM images also presents the interface between MMT sheets and $TiO_{2\text{-}NTs}$ as well as interface between $TiO_{2\text{-}NTs}$, which also allow to evaluate the connection, alignment and orientation of the $TiO_{2\text{-}NTs}$ in the MMT/$TiO_{2\text{-}NTs}$ photocatalyst.

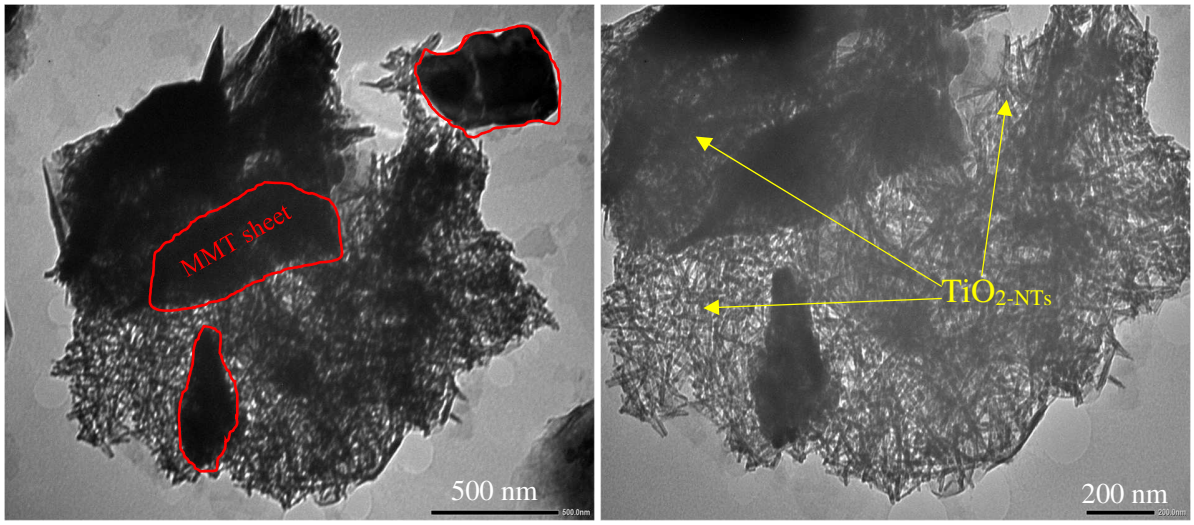

Figure 2: TEM images of MMT/$TiO_{2\text{-NTs}}$ at different magnifications

3.2. XRD diffraction of photocatalysts

The structure of MMT, TiO_2, MMT/TiO_2 and MMT/$TiO_{2\text{-NTs}}$ was also studied by X-ray diffraction as shown in Figure 3. The TiO_2 nanoparticles show the planes of anatase crystallization consisting of the diffraction peaks at (2θ) 25.3°; 37.9°; 47.8°; 54.3°; 55° and 62.7° corresponding to the network surfaces (101), (004), (200), (105), (211) and (204), respectively, with a strongest peak A(101). This structure corresponds to the highest photocatalytic activity of TiO_2 (Ayoubi-Feiz et al., 2014). For the MMT sample, it has the d_{001} spacing about 14.5 Å at (2θ) 6,1° and other diffraction peaks are observed at (2θ) 9.1°; 12.7°; 19.6°; 21.9°; 26.6°; and 35.0°. The two peaks at (2θ) 20.5° and 27.6° characterize the quartz structure in MMT, which is consistent with the literature (Szczepanik, 2017b).

The XRD pattern of MMT/TiO_2 nanocomposite shows the existence of mainly three phases: MMT at (2θ) 5-20°, SiO_2 at (2θ) 26.6° and anatase at (2θ) 25.3°, in which, the

phases MMT and SiO_2 are typical for MMT, and anatase represents for TiO_2. In addition, the d_{001} spacing of MMT at (2θ) 6.1° was shifted to an angle at (2θ) 6.3° in MMT/TiO_2 nanocomposite, which corresponds to d_{001} spacing to 14 Å. This result shows that the immobilization of TiO_2 nanoparticles on the surface of MMT (Khataee et al., 2015) and a small part of TiO_2 has entered inside the layer structure of the MMT.

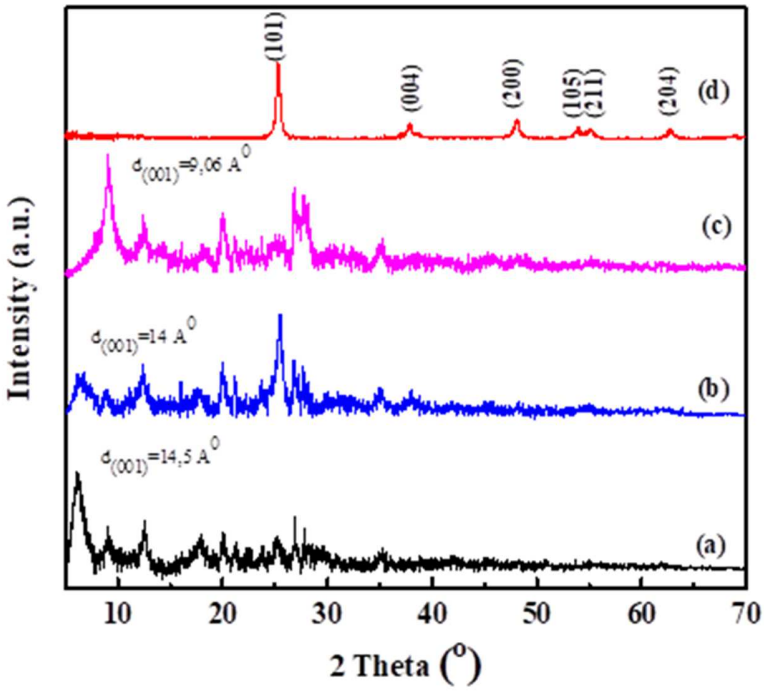

Figure 3. XRD diffraction patterns of different samples: (a) MMT; (b) nanocomposite MMT/TiO_2; (c) nanocomposite MMT/$TiO_{2\text{-NTs}}$; and (d) nano TiO_2

The XRD pattern of MMT/$TiO_{2\text{-NTs}}$ nanocomposite shows also the existence in three main phases as MMT/TiO_2 nanocomposite. However, the peak A (101) has a low intensity compared to that of TiO_2 sample, corresponding to a lower crystallization. This shows that during the hydrothermal process at 130°C, the crystal structure of $TiO_{2\text{-NTs}}$ has

been changed to reduce the anatase phase in TiO_2. Moreover, the d_{001} spacing of MMT was reduced to 9.06 Å corresponding to a larger angle (2θ) 9.2° compared to pure MMT and MMT/TiO_2 nanocomposite. This could be explained by the $TiO_{2\text{-}TNs}$ having entered the layer structure of MMT, leading to decrease the d_{001} spacing of MMT.

3.3. FTIR spectroscopy analysis of photocatalyst

Characterization of variations on functional groups and chemical bonds of TiO_2, $TiO_{2\text{-}NTs}$, pure MMT and their nanocomposites were evaluated through FTIR spectrum as shown in Figure 4. TiO_2 nanoparticles has only one peak at wavenumbers of 430 cm^{-1}, corresponding to stretching vibration of Ti-O, meanwhile $TiO_{2\text{-}NTs}$ have adsorption band at 460-908 cm^{-1} corresponding to stretching vibration of Ti-O band (Pang and Abdullah, 2013; Khataee et al., 2015). $TiO_{2\text{-}NTs}$ has also a peak at wavenumber of 1641 cm^{-1} could be attributed to interlayer H–O–H molecules (Wang et al., 2009). A wide-bulb peak at wavenumber of 3390 cm^{-1} characterizes for the stretching vibration of -OH group on surface of $TiO_{2\text{-}TNs}$.

The pure MMT has absorbance peaks at wavenumbers 3388 cm^{-1} and 3621 cm^{-1} that characterize the symmetrical stretching vibration of the -OH group of H_2O molecules absorbed in MMT. A vibration at wavenumber of 1639 cm^{-1} characterizes for deformation of interlayer H–O–H molecules. A strong peak at wavenumber of 987 cm^{-1} characterizes asymmetrical stretching vibration of -Si-O group. A peak at wavenumber of 789 cm^{-1} characteristics of Al-O stretching vibration, a peak at wavenumber of 524 cm^{-1} represents the Al–O–Si deformation vibration and a peak at wavenumber of 462 cm^{-1}

297 characteristics of Si–O–Si deformation (Liu et al., 2007; Aber et al., 2009; Khataee et al.,
298 2015).
299 In comparison to FTIR spectra of pure TiO_2, $TiO_{2\text{-NTs}}$, MMT and their nanocomposites, it
300 seems that component peaks are present in the FTIR spectra of nanocomposites. It is also
301 confirmed that the wide absorbance band of 462 – 789 cm^{-1} correspond to the adsorption
302 of Ti-O. However, they did not show the stretching vibration of Si-O-Ti at wavenumber
303 around 935 cm^{-1} (Iwasaki et al., 1994) as expected or this peak is overlapped with the
304 strong peak of MMT or this might be due to the small proportion of TiO_2 in MMT.

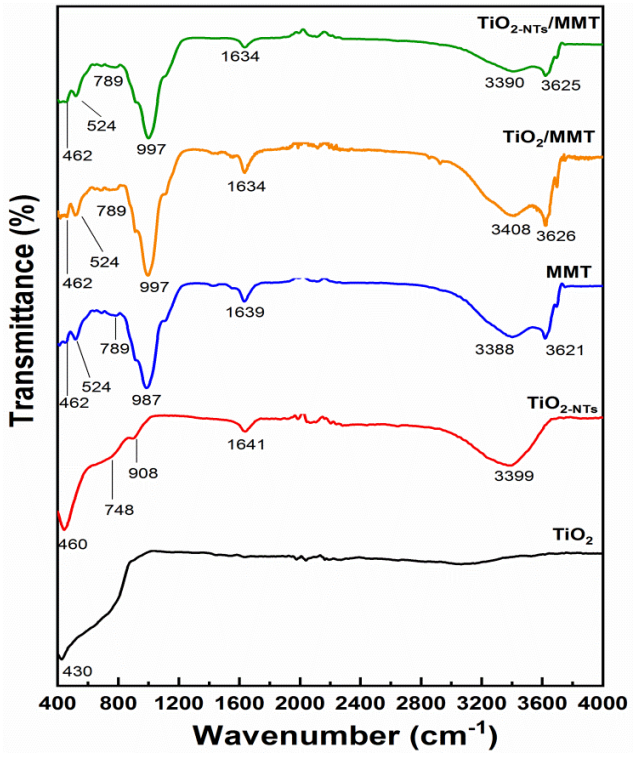

305

306 **Figure 4**. FT-IR spectra of different samples: (a) MMT, (b) nanocomposite MMT/TiO_2,
307 (c) nanocomposite MMT/$TiO_{2\text{-NTs}}$, (d) nano TiO_2 and (e) $TiO_{2\text{-NTs}}$
308
309

3.4. The chemical compositions of photocatalysts

The EXD results of MMT, MMT/TiO_2 and MMT/$TiO_{2\text{-NTs}}$ photocatalysts are shown in Figure 5. The chemical compositions of MMT include Al, C, Fe, K, Mg, Na, O, Si. The presence of elements K and Fe is due to the isomorphic substitution of metal cations such as K^+, Fe^{2+}. The EDX spectra of MMT/TiO_2 and MMT/$TiO_{2\text{-TNs}}$ photocatalyst show the same chemical compositions as MMT (Al, C, Fe, K, Mg, Na, O, Si) including the appearance of Ti element. This confirms the existence of Ti in these photocatalysts.

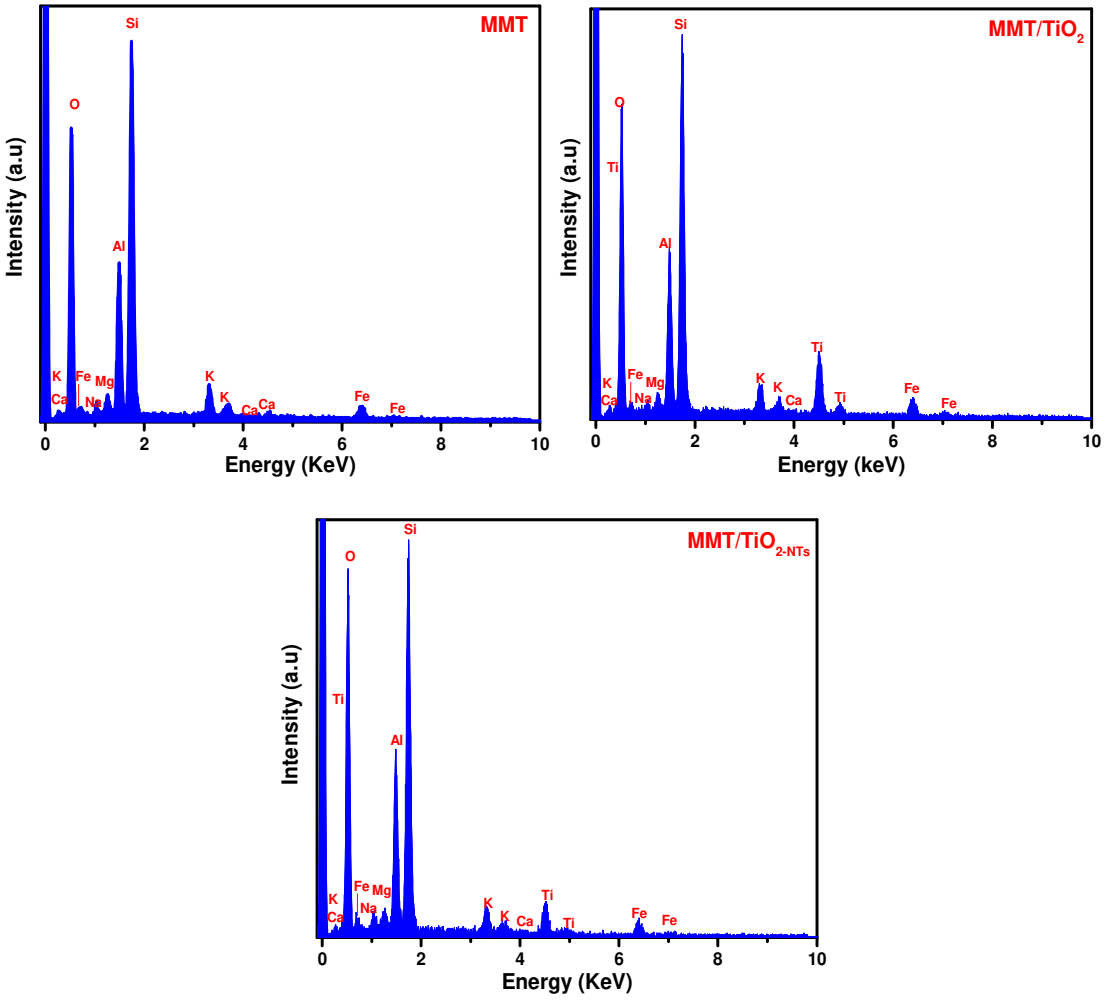

Figure 5: The EXD spectra of MMT, MMT/TiO_2, and MMT/$TiO_{2\text{-TNs}}$ photocatalysts

3.5. Photocatalytic performance of photocatalyst under UV-C irradiation

The photocatalytic performance of photocatalyst was determined through the photodegradation of rhodamine B by measuring the UV-Vis adsorption spectra in dark and UV-C irradiation. The UV-Vis adsorption spectra of rhodamine B at different concentrations are shown a linear of intensity absorbance peak with rhodamine B concentration with the maximum adsorption peak at a wavelength of 550 nm after 210 min of UV-C irradiation. This result also confirms that rhodamine B is not degraded under UV-C irradiation during exposition time. In addition, UV–Vis curves of rhodamine B (10 ppm) with photocatalyst under dark and UV-C irradiation conditions after 210 min are plotted in Figure 6a and 6b, respectively.

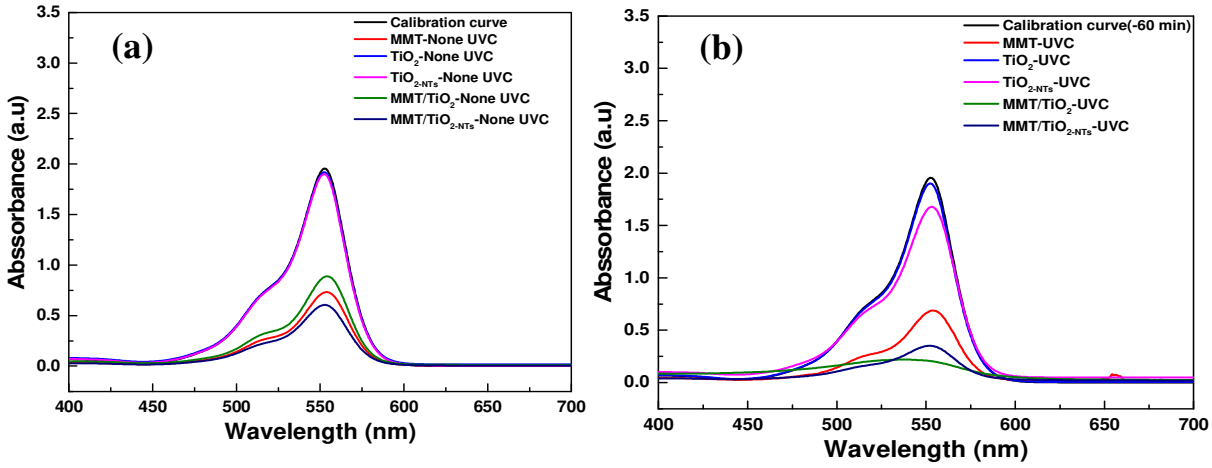

Figure 6: UV-Vis adsorption spectra of Rhodamine B: (a) 10 ppm rhodamine B with different photocatalysts under dark condition and (b) 10 ppm rhodamine B with different photocatalysts under UV-C irradiation condition after 210 min.

Accordingly, the photocatalytic activities and efficiencies of photocatalysts are calculated and exhibited in Figure 7. The photocatalytic activities in rhodamine B degradation of

MMT, TiO_2, $TiO_{2\text{-NTs}}$, MMT/TiO_2, and MMT/$TiO_{2\text{-NTs}}$ in dark condition is shown in Figure 7a. The adsorption capacity of TiO_2 and $TiO_{2\text{-NTs}}$ is very low and has equal efficiency (<10%). After incorporating with MMT, the adsorption efficiency is changed in the following order: MMT/TiO_2 <MMT <MMT/$TiO_{2\text{-NTs}}$. This result shows that, when incorporated to MMT, $TiO_{2\text{-NTs}}$ has demonstrated their capacity to absorb rhodamine B compared to that of MMT/TiO_2. In addition, adsorption equilibrium time of MMT, MMT/TiO_2, and MMT/$TiO_{2\text{-NTs}}$ photocatalysts is about 40, 60 and 60 min, respectively. The integration of TiO_2 and $TiO_{2\text{-NTs}}$ into MMT lead to increase in adsorption equilibrium time, which is probably due to the dispersion of TiO_2 particles and $TiO_{2\text{-TNs}}$ into MMT interlayers structure, reducing pores size, thereby extending the adsorption equilibrium time.

The influence of UV-C irradiation to trigger a photocatalytic effect likely to degrade rhodamine B of MMT, TiO_2, $TiO_{2\text{-TNs}}$ and their incorporation with MMT sheets is shown in Figure 7b. Firstly, it could be seen that the energy of UV-C irradiation alone is not enough to degrade rhodamine B. The rhodamine B degradation efficiency of MMT is the same without and within UV-C irradiation because MMT has only adsorption property without photocatalytic property. $TiO_{2\text{-NTs}}$ have higher photocatalytic efficiency to degrade rhodamine B than TiO_2 nanoparticles. In particular, the degradation efficiency of TiO_2 nanoparticles increased slightly to ca. 20%, corresponding to $C/C_0 = 0.8$ compared to less than 10% ($C/C_0 = 0.9$) without irradiation. Meanwhile, the efficiency of for $TiO_{2\text{-NTs}}$ increased significantly to 65% (C/C0 = 0.35) compared to less than 10% (0.9 C/C_0) of sample without UV-C irradiation. Thus, under UV-C irradiation, TiO_2 and $TiO_{2\text{-NTs}}$ are

able to absorb photon energy to form hydroxyl free radicals (•OH) free radicals, which are main factors to degrade rhodamine B.

The efficiency both MMT/TiO_2 and MMT/$TiO_{2\text{-NTs}}$ photocatalyst are also significantly increased under UV-C irradiation. It increased to 90% (C/C_0 = 0.1) with irradiation compared to 46% (C/C_0 = 0.54) in dark condition for MMT/TiO_2 photocatalyst. Similarly, it is recorded about 85% (C/C_0 = 0.15) compared to 73% (C/C_0 = 0.27) in dark condition for MMT/$TiO_{2\text{-NTs}}$ photocatalyst. Thus, the results showed that under UV-C irradiation, the photocatalytic effective of TiO_2 nanoparticles is increased through more production of free radicals (•OH), leading to capturing and degrading of rhodamine B molecules. In addition, efficiency of MMT/$TiO_{2\text{-NTs}}$ photocatalyst is lower than that of MMT/TiO_2. This is due to $TiO_{2\text{-NTs}}$ in tubular form, which was intertwined in layer structure of MMT sheets. This limits photon energy absorption of $TiO_{2\text{-TNs}}$, resulting in the less •OH free radical production, resulting in lower rhodamine B degradation efficiency.

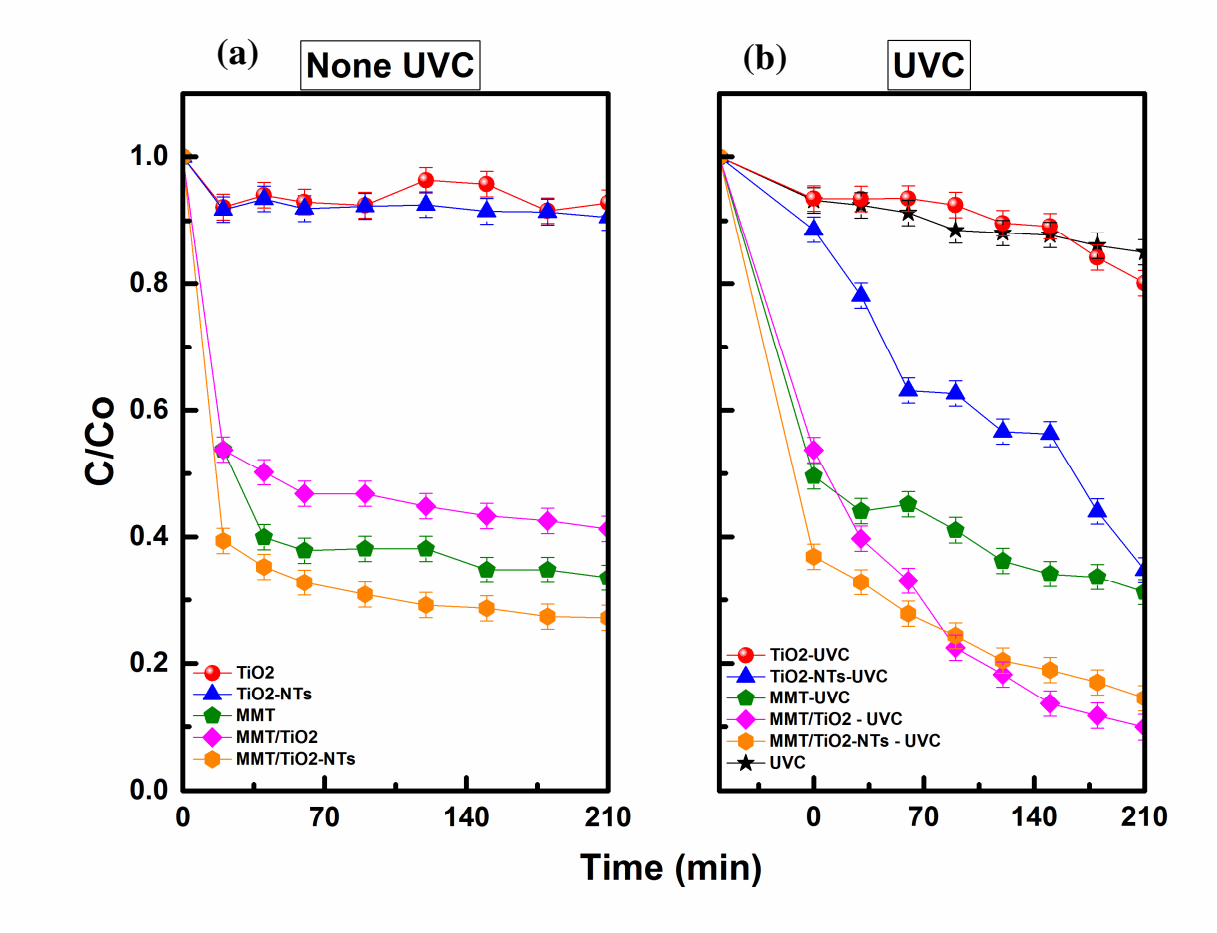

Figure 7: Photocatalytic degradation of rhodamine B with 10 ppm using different photocatalyst: (a) in the dark condition, (b) in the UV-C irradiation condition.

In addition, the photocatalytic performance of MMT/TiO_2 and MMT/$TiO_{2\text{-NTs}}$ to rhodamine B degradation is compared to that of the TiO_2 based photocatalyst in the literature as exhibited in Table 1. Thus, the photocatalytic performance of MMT/TiO_2 and MMT/$TiO_{2\text{-NTs}}$ have shown a superior efficiency in rhodamine B degradation compared to other TiO_2 based photocatalysts in the literature. Basically, the efficiency of rhodamine B degradation is dependent on many factors such as light source, rhodamine B concentration, and catalyst amount, etc. Indeed, these results suggest that the combination

382 of TiO_2 and $TiO_{2\text{-NTs}}$ with MMT has significantly increased the photocatalytic efficiency
383 to eliminate rhodamine B from dye effluent.

384 Table 1. Photocatalytic performance of TiO_2 and $TiO_{2\text{-NTs}}$ based photocatalyst to
385 rhodamine B degradation compared to previous studies

Catalyst	Light source	Concentration (mg/L) of rhodamine B	Catalyst amount (mg)	Degradation (%)	Exposed time (min)	Ref
TiO_2	UV-C lamp	10	10	20.0	210	this study
$TiO_{2\text{-NTs}}$	UV-C lamp	10	10	65.3	210	this study
MMT/TiO_2	UV-C lamp	10	10	90.0	210	this study
MMT/TiO_2	UV-C lamp	3	10	100	210	This study
MMT/$TiO_{2\text{-NTs}}$	UV-C lamp	10	10	85.5	210	this study
MMT/$TiO_{2\text{-NTs}}$	UV-C lamp	3	10	97.5	210	this study
10%MWCNT/TNT	HPMV lamp	50	50	89	60	(Natarajan et al., 2017)
V_2O_5/TiO_2	Visible	10	1.6 g/L	70	240	(Wang et al., 2012)
$BiVO_4/TiO_2$	Visible	1	-	85	120	(Hu et

						al., 2015)
Polyphyrin/TiO_2	Incandescent light	5	0.75 g/L	55.5	198	(Huang et al., 2009)
B-doped TiO_2	Stimulated sunlight	-	-	52	210	(Li et al., 2013)
g-C_3N_4/TiO_2	Visible	1		90	78	(Hao et al., 2016)

The reusability of MMT/TiO_2 and MMT/$TiO_{2\text{-NTs}}$ for the rhodamine B degradation was performed by repeating the reaction for three cycles using the recovered photocatalyst under the same conditions, as shown in Figure 8. After three consecutive runs, the photocatalytic activity of MMT/TiO_2 was decreased by 18% and the photocatalytic activity of MMT/$TiO_{2\text{-NTs}}$ was decreased by 23.5%. This might be ascribed to the accumulation of photodegradation products and rhodamine B molecules on the catalyst surface which resulted in decreasing the active sites (Pannak et al., 2018).

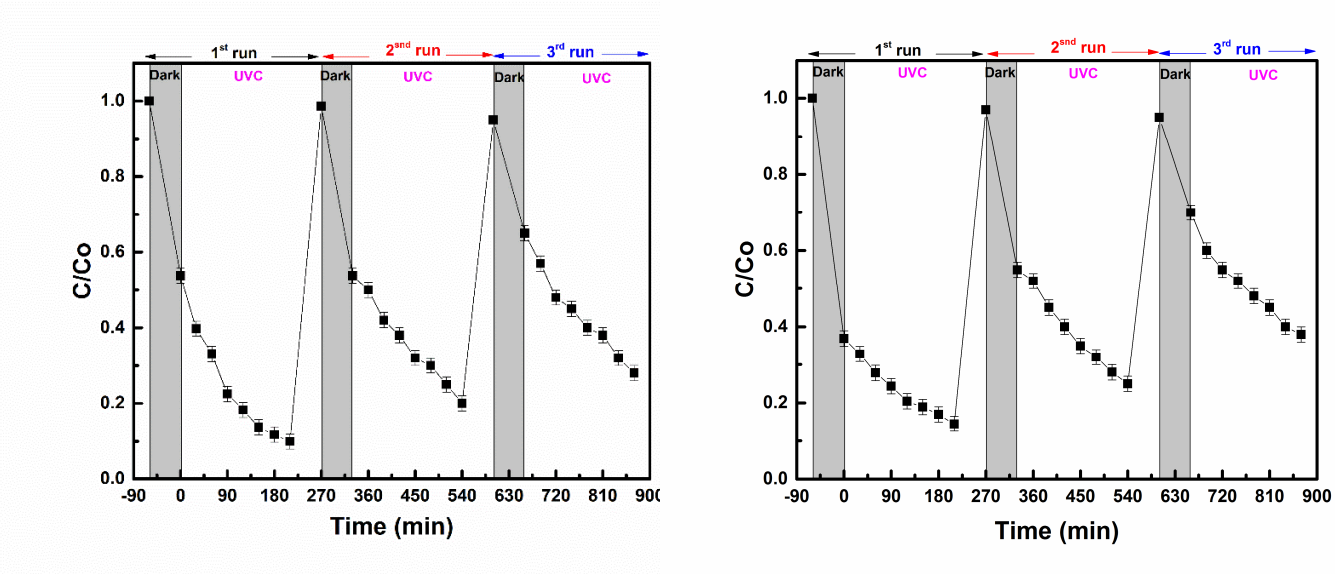

Figure 8: Photocatalytic activity of (a) MMT/TiO_2 and (b) MMT/$TiO_{2\text{-NTs}}$ photocatalyst for three consecutive runs with10 ppm rhodamine B.

3.6. Photocatalytic performance at different rhodamine B concentrations

The photocatalytic effectiveness of MMT/TiO_2 and MMT/$TiO_{2\text{-NTs}}$ photocatalysts to degrade rhodamine B at different concentrations under UV-C irradiation is depicted in Figure 9. The weight of photocatalyst for each experiment is 10 mg. The results show that MMT/TiO_2 photocatalyst has a higher photocatalytic efficiency to degrade rhodamine B than that of MMT/$TiO_{2\text{-NTs}}$ photocatalyst for all rhodamine B concentrations. In particular, the degradation efficiency of MMT/TiO_2 photocatalyst is recorded at 100%, 97.5%, 90.1%, 74.8% and 70.1% corresponding to concentration at 3 ppm, 6 ppm, 11 ppm, 16 ppm and 18 ppm, respectively. Whereas, these values of $TiO_{2\text{-TNs}}$/MMT photocatalyst are recorded at 97.5%, 90.5%, 85.5%, 61.2% and 52.6%, for the same concentrations. However, it could be seen that MMT/$TiO_{2\text{-NTs}}$ photocatalyst

421 presents a decreased efficiency at long term but seems to be slightly higher efficient at
422 short term for low concentration of rhodamine B. This is probably the dominant effect of
423 the $TiO_{2\text{-}TNs}$ located on the surface of MMT sheets. In general, at increasing rhodamine B
424 concentrations, the photocatalytic activity and degradation efficiency of TiO_2/MMT and
425 $TiO_{2\text{-}NTs}$/MMT photocatalysts decreases because of the smaller length of penetration of
426 UV in the rhodamine B solution. This means that rhodamine B molecules are adsorbed
427 onto the surface of MMT/TiO_2 and MMT/$TiO_{2\text{-}TNs}$ photocatalysts, which interferes with
428 the photon energy exposure of TiO_2 and $TiO_{2\text{-}TNs}$ on MMT surface, leading to decrease in
429 photocatalytic ability to rhodamine B degradation. In addition, it could be observed that
430 there are the combined effects; at high rhodamine B concentration, the adsorption of
431 rhodamine B by MMT is saturated, which can be seen by the attenuation observed at
432 short time. But we can still see the better effect of MMT/TiO_2 to degrade rhodamine B
433 over time, which is much less pronounced with MMT/$TiO_{2\text{-}NTs}$.

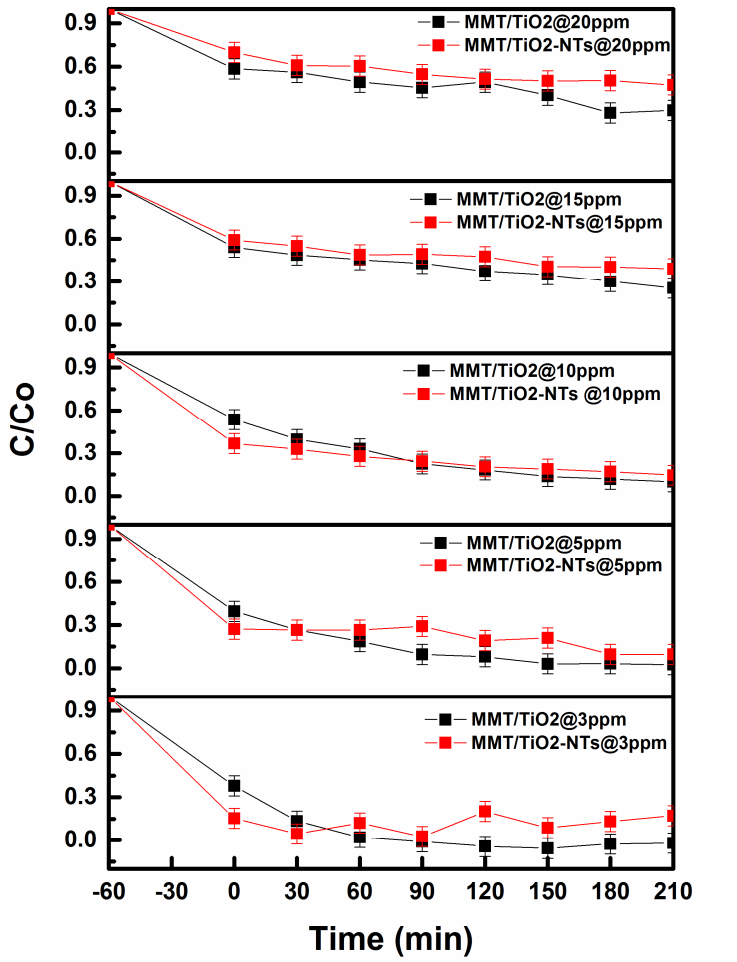

434

435 **Figure 9**. Degradation effectiveness of MMT/TiO_2 and MMT/$TiO_{2\text{-NTs}}$ photocatalysts at

436 different concentrations of rhodamine B under UV-C irradiation.

437

438 ### 3.7. The mechanism of rhodamine B degradation of photocatalyst

439 The mechanism of rhodamine B degradation by photocatalysts is proposed in Figure 10.

440 The TiO_2 components of MMT/TiO_2 act as photocatalyst. Initially, the UV-C irradiation

441 source produced high-energy photons activates to create photoinduced electrons (e^-) and

442 leave holes (h^+) of the TiO_2. The negatively charged electrons are excited to cross the

443 band gap (E_g) and jump into the conduction band (CB) leaving holes with positively

charged charges in the valence region (VB). In the presence of MMT, the generated electrons move to the empty d-orbital of the metals in MMT structure. This electron transfer process can prevent the e^- - h^+ pair from recombination. Then, electrons trapped in MMT react with O_2 to produce free superoxide radicals ($^{\bullet}O_2^-$) (Xu et al., 2021). At the same time, photogenerated holes react with H_2O or the adsorbed hydroxyl ions (OH^-) molecules to produce hydroxyl radicals ($^{\bullet}OH$) (Sun et al., 2021). Finally, the produced free radicals ($^{\bullet}OH$, $^{\bullet}O_2^-$, h+) with strong oxidizing ability will degrade rhodamine B molecules into degradation products (Wang et al., 2020; E et al., 2021). Thus, the free radicals (•OH and $•O_2^-$) attack the central carbon in the rhodamine B molecules and oxidize them to low-weight intermediates, which results in the formation of small and broken-ring compounds. In addition, the smaller compounds are degraded to CO_2 and H_2O (Isari et al., 2018). All steps of photocatalytic process to degrade rhodamine B are summarized in following equations (1-5):

$$TiO_2 + h\nu \rightarrow TiO_2\ (e^- + h^+) \quad (1)$$

$$TiO_2\ (e^- + h^+) + MMT \rightarrow TiO_2\ (h^+) + MMT\ (e^-) \quad (2)$$

$$TiO_2\ (h^+) + OH^- \rightarrow TiO_2 + {}^{\bullet}OH \quad (3)$$

$$MMT\ (e^-) + O_2 \rightarrow MMT + {}^{\bullet}O_2^- \quad (4)$$

$$•O_2^- + H_2O \rightarrow {}^{\bullet}OH + H^+ \quad (5)$$

$$h^+ + OH^- \rightarrow {}^{\bullet}OH \quad (6)$$

$$^{\bullet}OH/^{\bullet}O_2^-/h^+ \text{ radicals + rhodamine B} \rightarrow \text{degradation products} \quad (7)$$

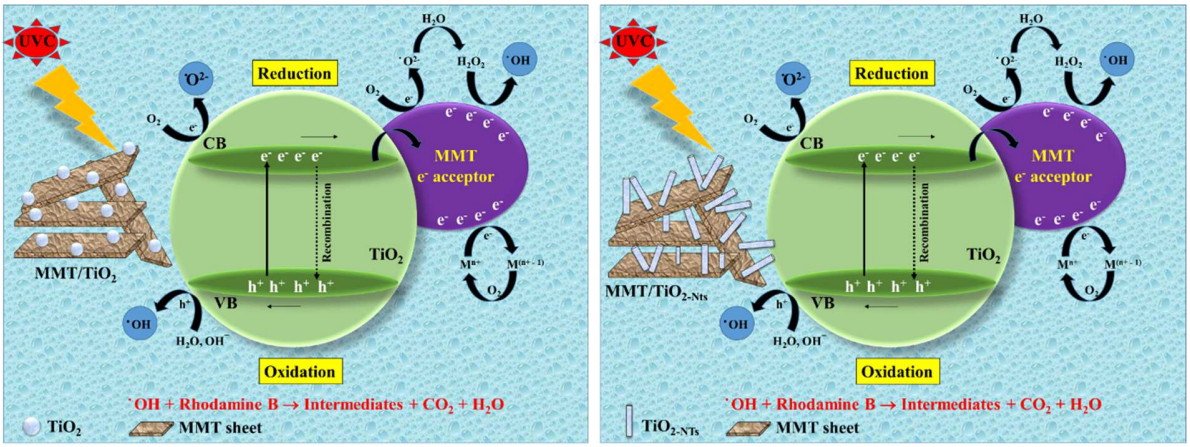

Figure 10: The photocatalytic mechanism of MMT/TiO_2 (left) and MMT/$TiO_{2\text{-NTs}}$ (right) photocatalysts for rhodamine B degradation.

The degradation products with rhodamine B for at 30 min during photocatalytic process were investigated using LC-MS spectrum and presented in Figure 11. Firstly, the rhodamine B (A_1, m/z 443) was attacked by a large number of e-, which was created by MMT/TiO_2 or MMT/$TiO_{2\text{-NTs}}$, to produce N, N, N-diethyl-N'-ethylrhodamine (A_2, m/z 415) (Wermuth et al., 2019). Then, A_2 was degraded into two isomers N, N'-ethyl-ethylrhodamine (A_3, m/z 388) and N, N- diethyl-rhodamine (A_4, m/z 388) (Hegazey et al., 2020). Next, A_3 and A_4 were degraded into N, N'-monomethyl-ethylrhodamine (A_5, m/z 360) and N, N'-ethylrhodamine (A_6, m/z 332) (E et al., 2021). Then, –NH bond of A6 was broken to form N'-ethylrhodamine (A_7, m/z 317) and 2-(3H-xanthen-9-yl) benzoic acid (A_8, m/z 302) was generated when all –NH bonds were broken (E et al., 2021). 9-phenyl-3H-xanthene (A_9, m/z 257) was produced by breaking carboxyl group from A8. The degradation products were

benzoic acid (A_{10}, m/z 123) (Guo et al., 2020). Finally, A_{10} was degraded by h^+, $^{\bullet}O_2$ and $^{\bullet}OH$ to produce CO_2 and H_2O (Hegazey et al., 2020).

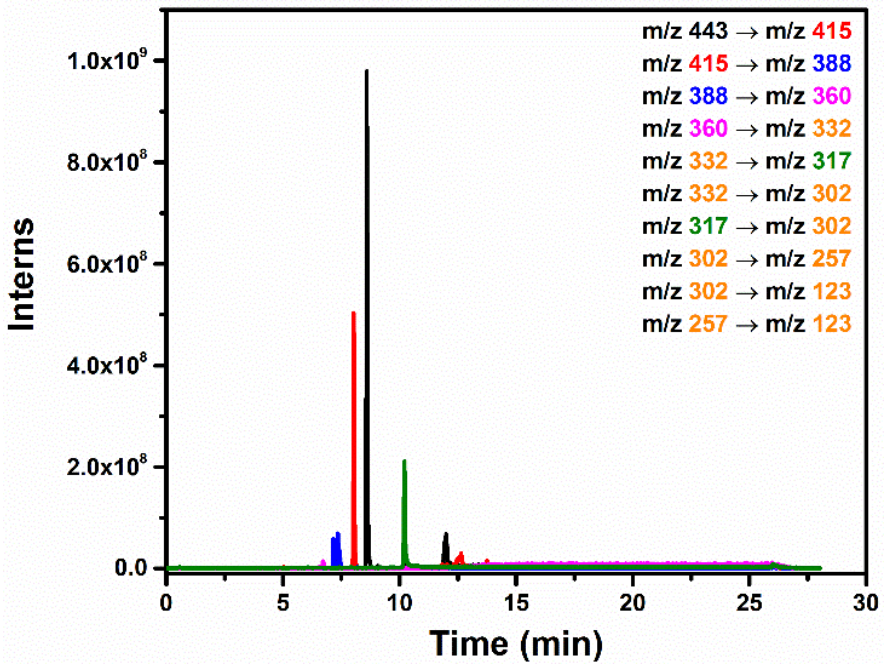

Figure 11. LC-MS spectrum of degradation products with Rh-B for at 30 min during photocatalytic process

In addition, under the UVC irradiation, $TiO_{2\text{-NTs}}$ exhibits a higher photocatalytic capacity than TiO_2. However, the decomposition efficiency of MMT/$TiO_{2\text{-NTs}}$ is lower than that of MMT/TiO_2. This suggests that the addition of $TiO_{2\text{-NTs}}$ into MMT leads to decrease the photocatalytic activity of $TiO_{2\text{-NTs}}$. This is due to the MMT has layer structure, when $TiO_{2\text{-NTs}}$ are intercalated into MMT layers, the inner surface is not adequately illuminated by UV-C irradiation as described in Figure 12.

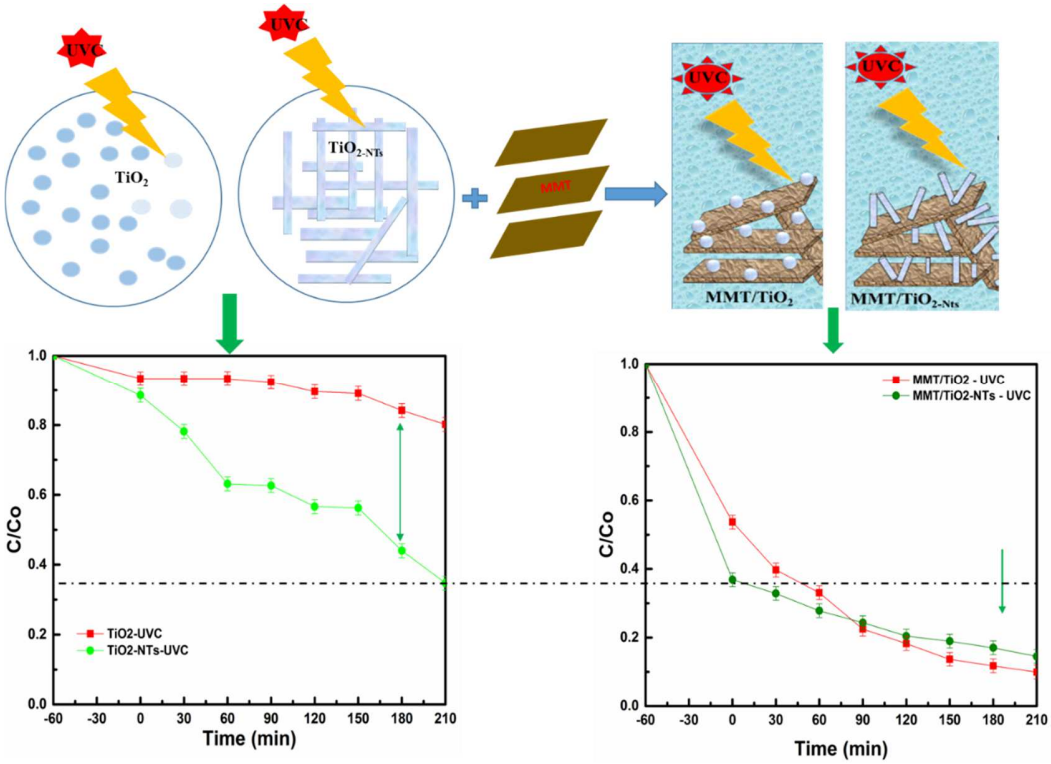

Figure 12: The illustration of photocatalytic activities of MMT/TiO_2 and MMT/$TiO_{2\text{-}NTs}$ for rhodamine B degradation under UV-C irradiation.

Therefore, the number of absorbed photons of $TiO_{2\text{-}NTs}$ inside is less than the outer surface, affecting the chemical transformation of the photocatalytic process. Therefore, the photocatalytic ability of $TiO_{2\text{-}NTs}$ is limited in incorporation with MMT sheets although they have better photocatalytic effectively than TiO_2 nanoparticles.

4. Conclusions

In this study, bentonite mineral is purified to produce MMT clay that has good property of organic dye absorption but no photocatalytic activity. In addition, random-orientation $TiO_{2\text{-}NTs}$ were successfully synthesized by a low-cost hydrothermal method. As-synthesized $TiO_{2\text{-}NTs}$ were demonstrated to present much more efficient photodegradation

of rhodamine B dye in comparison with commercial TiO_2 nanoparticle photocatalyst. However, the efficiency of rhodamine B degradation under UVC light of MMT/TiO_2 is higher than that of MMT/$TiO_{2\text{-NTs}}$. This is due to the immobilization of TiO_2 nanoparticles at the surface of MMT sheets, so they are available for UVC light absorption. Besides, the effectiveness of $TiO_{2\text{-NTs}}$ is lost in the presence of MMT because $TiO_{2\text{-NTs}}$ intercalate into the MMT layers, leading to the inhibition of UVC light absorption. Moreover, MMT/$TiO_{2\text{-NTs}}$ nanocomposite still shows a better rhodamine B removal effectiveness in the initial period of 1 hour under UVC light irradiation. As a result, the combination of MMT and $TiO_{2\text{-NTs}}$ can be applied for water treatment in short time. The photocatalytic performance of MMT/TiO_2 reached to 100% for 3ppm and 90% at 10ppm of rhodamine B, while these values are 97.5% and 85.5%, respectively, recorded for MMT/$TiO_{2\text{-NTs}}$.

Declarations of interest: none.

Acknowledgments:

This research was supported by Vietnam National University Ho Chi Minh City (VNU-HCM) [grant number C2021]. The authors would like to thank Departement de la Marne, Greater Reims, Region Grand Est and European Union with European Regional Development Fund (ERDF Champagne Ardenne 2014-2020) for their financial support to the Chair of Biotechnology of CentraleSupélec.

References

Abdi, J., Vossoughi, M., Mahmoodi, N.M., Alemzadeh, I., 2017. Synthesis of metal-organic framework hybrid nanocomposites based on GO and CNT with high adsorption capacity for dye removal. Chemical Engineering Journal 326, 1145-1158.

Aber, S., Khataee, A., Sheydaei, M., 2009. Optimization of activated carbon fiber preparation from Kenaf using K2HPO4 as chemical activator for adsorption of phenolic compounds. Bioresource Technology 100, 6586-6591.

Ayoubi-Feiz, B., Aber, S., Khataee, A., Alipour, E.J., 2014. Electrosorption and photocatalytic one-stage combined process using a new type of nanosized TiO 2/activated charcoal plate electrode. Environmental Science Pollution Research 21, 8555-8564.

Bing, H., Qi, D., Jie, C., Wei, F., Suling, L., He-li, W., 2015. Photocatalytic Degradation of Methyl Orange Over Y3+ Doped TiO2 Pillared Montmorillonite. Journal of Advanced Oxidation Technologies 18, 98-104.

Casu, A., Lamberti, A., Stassi, S., Falqui, A., 2018. Crystallization of TiO_2 Nanotubes by In Situ Heating TEM. Nanomaterials (Basel) 8, 40.

Charumathi, D., Das, N., 2012. Packed bed column studies for the removal of synthetic dyes from textile wastewater using immobilised dead C. tropicalis. Desalination 285, 22-30.

Cheng, L., Zhang, D., Liao, Y., Li, F., Zhang, H., Xiang, Q., 2019. Constructing functionalized plasmonic gold/titanium dioxide nanosheets with small gold nanoparticles

for efficient photocatalytic hydrogen evolution. Journal of Colloid and Interface Science 555, 94-103.

Chinh, V.D., Broggi, A., Di Palma, L., Scarsella, M., Speranza, G., Vilardi, G., Thang, P.N., 2018. XPS Spectra Analysis of Ti2+, Ti3+ Ions and Dye Photodegradation Evaluation of Titania-Silica Mixed Oxide Nanoparticles. Journal of Electronic Materials 47, 2215-2224.

Chinh, V.D., Hung, L.X., Di Palma, L., Hanh, V.T.H., Vilardi, G., 2019. Effect of Carbon Nanotubes and Carbon Nanotubes/Gold Nanoparticles Composite on the Photocatalytic Activity of TiO2 and TiO2-SiO2. Chemical Engineering & Technology 42, 308-315.

Cui, L., Hui, K., Hui, K., Lee, S., Zhou, W., Wan, Z., Thuc, C.-N.H.J.M.L., 2012. Facile microwave-assisted hydrothermal synthesis of TiO2 nanotubes. Materials Letters 75, 175-178.

Dao, M.U., Le, H.S., Hoang, H.Y., Tran, V.A., Doan, V.D., Le, T.T.N., Sirotkin, A., Le, V.T., 2020. Natural core-shell structure activated carbon beads derived from Litsea glutinosa seeds for removal of methylene blue: Facile preparation, characterization, and adsorption properties. Environmental Research, 110481.

Diamond, S.A., Kennedy, A.J., Melby, N.L., Moser, R.D., Poda, A.R., Weiss, C.A., Brame, J.A., 2017. Assessment of the potential hazard of nano-scale TiO2 in photocatalytic cement: application of a tiered assessment framework. NanoImpact 8, 11-19.

581 dos Santos, A.B., Cervantes, F.J., van Lier, J.B., 2007. Review paper on current
582 technologies for decolourisation of textile wastewaters: Perspectives for anaerobic
583 biotechnology. Bioresource Technology 98, 2369-2385.
584 E, T., Xiao, X., Yang, S., 2021. A new synthesizing method of TiO2 with
585 montmorillonite: Effective photoelectron transfer to degrade Rhodamine B. Separation
586 and Purification Technology 258, 118070.
587 Fan, L., Long, J., Gu, Q., Huang, H., Lin, H., Wang, X., 2014. Single-site nickel-grafted
588 anatase TiO2 for hydrogen production: Toward understanding the nature of visible-light
589 photocatalysis. Journal of Catalysis 320, 147-159.
590 Farghali, A.A., Zaki, A.H., Khedr, M.H., 2014. Hydrothermally synthesized TiO2
591 nanotubes and nanosheets for photocatalytic degradation of color yellow sunset.
592 International Journal of Advanced Research 2, 285-291.
593 Guo, N., Liu, H., Fu, Y., Hu, J., 2020. Preparation of Fe2O3 nanoparticles doped with
594 In2O3 and photocatalytic degradation property for rhodamine B. Optik 201, 163537.
595 Gupta, V.K., Suhas, 2009. Application of low-cost adsorbents for dye removal – A
596 review. Journal of Environmental Management 90, 2313-2342.
597 Habila, M.A., Alothman, Z.A., El-Toni, A.M., Labis, J.P., Soylak, M., 2016. Synthesis
598 and application of Fe3O4@SiO2@TiO2 for photocatalytic decomposition of organic
599 matrix simultaneously with magnetic solid phase extraction of heavy metals prior to ICP-
600 MS analysis. Talanta 154, 539-547.

601 Hao, R., Wang, G., Tang, H., Sun, L., Xu, C., Han, D., 2016. Template-free preparation
602 of macro/mesoporous g-C3N4/TiO2 heterojunction photocatalysts with enhanced visible
603 light photocatalytic activity. Applied Catalysis B-environmental 187, 47-58.
604 Hassani, A., Khataee, A., Karaca, S., Fathinia, M., 2016. Heterogeneous photocatalytic
605 ozonation of ciprofloxacin using synthesized titanium dioxide nanoparticles on a
606 montmorillonite support: parametric studies, mechanistic analysis and intermediates
607 identification. RSC Advances 6, 87569-87583.
608 Hassani, A., Khataee, A., Karaca, S., Karaca, C., Gholami, P., 2017. Sonocatalytic
609 degradation of ciprofloxacin using synthesized TiO2 nanoparticles on montmorillonite.
610 Ultrasonics Sonochemistry 35, 251-262.
611 Hegazey, R.M., Abdelrahman, E.A., Kotp, Y.H., Hameed, A.M., Subaihi, A., 2020.
612 Facile fabrication of hematite nanoparticles from Egyptian insecticide cans for efficient
613 photocatalytic degradation of rhodamine B dye. Journal of Materials Research and
614 Technology 9, 1652-1661.
615 Hu, Y., Li, D.Z., Wang, H.B., Zeng, G.P., Li, X.H., Shao, Y., 2015. Role of active
616 oxygen species in the liquid-phase photocatalytic degradation of RhB using BiVO4/TiO2
617 heterostructure under visible light irradiation. J. Mol. Catal. A-Chem. 408, 172-178.
618 Huang, H., Gu, X., Zhou, J., Ji, K., Liu, H., Feng, Y., 2009. Photocatalytic degradation of
619 Rhodamine B on TiO2 nanoparticles modified with porphyrin and iron-porphyrin.
620 Catalysis Communications 11, 58-61.
621 Huang, J., Shi, Z., Dong, X., 2016. Nickel sulfide modified TiO2 nanotubes with highly
622 efficient photocatalytic H2 evolution activity. Journal of Energy Chemistry 25, 136-140.

623 Isari, A.A., Payan, A., Fattahi, M., Jorfi, S., Kakavandi, B., 2018. Photocatalytic
624 degradation of rhodamine B and real textile wastewater using Fe-doped TiO2 anchored
625 on reduced graphene oxide (Fe-TiO2/rGO): Characterization and feasibility, mechanism
626 and pathway studies. Applied Surface Science 462, 549-564.
627 Iwasaki, M., Yasumori, A., Shibata, S., Yamane, M., 1994. Preparation of high
628 homogeneity BaO-TiO2-SiO2 gel. Journal of Sol-Gel Science and Technology 2, 387-
629 391.
630 Katheresan, V., Kansedo, J., Lau, S.Y., 2018. Efficiency of various recent wastewater
631 dye removal methods: A review. Journal of Environmental Chemical Engineering 6,
632 4676-4697.
633 Khataee, A., Sheydaei, M., Hassani, A., Taseidifar, M., Karaca, S., 2015. Sonocatalytic
634 removal of an organic dye using TiO2/Montmorillonite nanocomposite. Ultrasonics
635 Sonochemistry 22, 404-411.
636 Kingsley, J.J., Suresh, K., Patil, K.C., 1990. Combustion synthesis of fine particle rare
637 earth orthoaluminates and yttrium aluminum garnet. Journal of Solid State Chemistry 88,
638 435-442.
639 Leong, S., Razmjou, A., Wang, K., Hapgood, K., Zhang, X., Wang, H., 2014. TiO2 based
640 photocatalytic membranes: A review. Journal of Membrane Science 472, 167-184.
641 Li, L., Yang, Y., Liu, X., Fan, R., Shi, Y., Shuo, L., Zhang, L., Fan, X., Tang, P., Rui, X.,
642 Zhang, W., Wang, Y., Ma, L., 2013. A direct synthesis of B-doped TiO2 and its
643 photocatalytic performance on degradation of RhB. Applied Surface Science 265, 36-40.

644 Liu, J., Li, X., Zuo, S., Yu, Y., 2007. Preparation and photocatalytic activity of silver and
645 TiO2 nanoparticles/montmorillonite composites. Applied Clay Science 37, 275-280.
646 Low, J., Zhang, L., Tong, T., Shen, B., Yu, J., 2018. TiO2/MXene Ti3C2 composite with
647 excellent photocatalytic CO2 reduction activity. Journal of Catalysis 361, 255-266.
648 Ma, X., Xiang, Q., Liao, Y., Wen, T., Zhang, H., 2018. Visible-light-driven CdSe
649 quantum dots/graphene/TiO2 nanosheets composite with excellent photocatalytic activity
650 for E. coli disinfection and organic pollutant degradation. Applied Surface Science 457,
651 846-855.
652 Malato, S., Fernández-Ibáñez, P., Maldonado, M.I., Blanco, J., Gernjak, W., 2009.
653 Decontamination and disinfection of water by solar photocatalysis: Recent overview and
654 trends. Catalysis Today 147, 1-59.
655 Mishra, A., Sharma, M., Mehta, A., Basu, S., 2017. Microwave Treated Bentonite Clay
656 Based TiO2 Composites: An Efficient Photocatalyst for Rapid Degradation of Methylene
657 Blue. Journal of nanoscience and nanotechnology 17, 1149-1155.
658 Nagaraja, R., Kottam, N., Girija, C.R., Nagabhushana, B.M., 2012. Photocatalytic
659 degradation of Rhodamine B dye under UV/solar light using ZnO nanopowder
660 synthesized by solution combustion route. Powder Technology 215-216, 91-97.
661 Natarajan, T.S., Lee, J.Y., Bajaj, H.C., Jo, W.-K., Tayade, R.J., 2017. Synthesis of
662 multiwall carbon nanotubes/TiO2 nanotube composites with enhanced photocatalytic
663 decomposition efficiency. Catalysis Today 282, 13-23.

664 Natarajan, T.S., Thomas, M., Natarajan, K., Bajaj, H.C., Tayade, R.J., 2011. Study on
665 UV-LED/TiO2 process for degradation of Rhodamine B dye. Chemical Engineering
666 Journal 169, 126-134.
667 Nguyen Van, H., Chu Van, H., Luu Hoang, T., Vo Nguyen, D.K., Ha Thuc, C.N., 2020.
668 The starch modified montmorillonite for the removal of Pb(II), Cd(II) and Ni(II) ions
669 from aqueous solutions. Arabian Journal of Chemistry 13, 7212-7223.
670 Niu, X., Sun, L., Zhang, X., Sun, Y., Wang, J., 2020. Fabrication and antibacterial
671 properties of cefuroxime-loaded TiO(2) nanotubes. Applied microbiology and
672 biotechnology 104, 2947-2955.
673 Pang, Y.L., Abdullah, A.Z., 2013. Effect of carbon and nitrogen co-doping on
674 characteristics and sonocatalytic activity of TiO2 nanotubes catalyst for degradation of
675 Rhodamine B in water. Chemical Engineering Journal 214, 129-138.
676 Pannak, P., Songsasen, A., Foytong, W., Kidkhunthod, P., Sirisaksoontorn, W., 2018.
677 Homogeneous distribution of nanosized ZnO in montmorillonite clay sheets for the
678 photocatalytic enhancement in degradation of Rhodamine B. Research on Chemical
679 Intermediates 44, 6861-6875.
680 Park, D.J., Sekino, T., Tsukuda, S., Hayashi, A., Kusunose, T., Tanaka, S.-I., 2011.
681 Photoluminescence of samarium-doped TiO2 nanotubes. Journal of Solid State
682 Chemistry 184, 2695-2700.
683 Rauf, M.A., Salman Ashraf, S., 2012. Survey of recent trends in biochemically assisted
684 degradation of dyes. Chemical Engineering Journal 209, 520-530.

685 Robinson, T., McMullan, G., Marchant, R., Nigam, P., 2001. Remediation of dyes in
686 textile effluent: a critical review on current treatment technologies with a proposed
687 alternative. Bioresource Technology 77, 247-255.
688 Sasani, A., Baktash, A., Mirabbaszadeh, K., Khoshnevisan, B., 2016. Structural and
689 electronic properties of Mg and Mg-Nb co-doped TiO2 (101) anatase surface. Applied
690 Surface Science 384, 298-303.
691 Shan, R., Lu, L., Gu, J., Zhang, Y., Yuan, H., Chen, Y., Luo, B., 2020. Photocatalytic
692 degradation of methyl orange by Ag/TiO2/biochar composite catalysts in aqueous
693 solutions. Materials Science in Semiconductor Processing 114, 105088.
694 Shi, L., Liang, L., Ma, J., Meng, Y., Zhong, S., Wang, F., Sun, J., 2014. Highly efficient
695 visible light-driven Ag/AgBr/ZnO composite photocatalyst for degrading Rhodamine B.
696 Ceramics International 40, 3495-3502.
697 Shiding Miao, Zhimin Liu, Buxing Han, Jianling Zhang, Xin Yu, Jimin Du, Zhenyu Sun,
698 2016. Synthesis and characterization of TiO2–montmorillonite nanocomposites and their
699 application for removal of methylene blue. Journal of Materials Chemistry 16, 579-584.
700 Sun, B., Qiu, P., Liang, Z., Xue, Y., Zhang, X., Yang, L., Cui, H., Tian, J., 2021. The
701 fabrication of 1D/2D CdS nanorod@Ti3C2 MXene composites for good photocatalytic
702 activity of hydrogen generation and ammonia synthesis. Chemical Engineering Journal
703 406, 127177.
704 Szczepanik, B., 2017a. Photocatalytic degradation of organic contaminants over clay-
705 TiO2 nanocomposites: A review. Applied Clay Science 141, 227-239.

706 Szczepanik, B., 2017b. Photocatalytic degradation of organic contaminants over clay-TiO
707 2 nanocomposites: A review. Applied Clay Science 141, 227-239.
708 Tahir, M., Amin, N.S., 2016. Performance analysis of nanostructured NiO–In2O3/TiO2
709 catalyst for CO2 photoreduction with H2 in a monolith photoreactor. Chemical
710 Engineering Journal 285, 635-649.
711 Thuc, C.-N.H., Grillet, A.-C., Reinert, L., Ohashi, F., Thuc, H.H., Duclaux, L., 2010.
712 Separation and purification of montmorillonite and polyethylene oxide modified
713 montmorillonite from Vietnamese bentonites. Applied Clay Science 49, 229-238.
714 Wang, H., Wang, H.-L., Jiang, W.-F., Li, Z.-Q., 2009. Photocatalytic degradation of 2,4-
715 dinitrophenol (DNP) by multi-walled carbon nanotubes (MWCNTs)/TiO2 composite in
716 aqueous solution under solar irradiation. Water Research 43, 204-210.
717 Wang, R., Shi, M., Xu, F., Qiu, Y., Zhang, P., Shen, K., Zhao, Q., Yu, J., Zhang, Y.,
718 2020. Graphdiyne-modified TiO2 nanofibers with osteoinductive and enhanced
719 photocatalytic antibacterial activities to prevent implant infection. Nature
720 Communications 11, 4465.
721 Wang, Y., Zhang, J., Liu, L., Zhu, C., Liu, X., Su, Q., 2012. Visible light photocatalysis
722 of V2O5/TiO2 nanoheterostructures prepared via electrospinning. Materials Letters 75,
723 95-98.
724 Wermuth, T.B., Arcaro, S., Venturini, J., Hubert Ribeiro, T.M., de Assis Lawisch
725 Rodriguez, A., Machado, E.L., Franco de Oliveira, T., Franco de Oliveira, S.E., Baibich,
726 M.N., Bergmann, C.P., 2019. Microwave-synthesized KNbO3 perovskites: photocatalytic
727 pathway on the degradation of rhodamine B. Ceramics International 45, 24137-24145.

728 Wong, C.L., Tan, Y.N., Mohamed, A.R., 2011. A review on the formation of titania
729 nanotube photocatalysts by hydrothermal treatment. Journal of Environmental
730 Management 92, 1669-1680.
731 Xu, R., Wei, N., Li, Z., Song, X., Li, Q., Sun, K., Yang, E., Gong, L., Sui, Y., Tian, J.,
732 Wang, X., Zhao, M., Cui, H., 2021. Construction of hierarchical 2D/2D Ti3C2/MoS2
733 nanocomposites for high-efficiency solar steam generation. Journal of Colloid and
734 Interface Science 584, 125-133.
735 Xu, X., Zhou, X., Li, X., Yang, F., Jin, B., Xu, T., Li, G., Li, M., 2014. Electrodeposition
736 synthesis of MnO2/TiO2 nanotube arrays nanocomposites and their visible light
737 photocatalytic activity. Materials Research Bulletin 59, 32-36.
738 Yin, J., Guo, H., Liu, Y., Kong, Y., Xia, X., Yao, L., Su, B., Wang, Y., Cao, Y., 2014.
739 Effect of MMT content on structure of polyimide/(TiO2+MMT) nanocomposite films.
740 2014 9th International Forum on Strategic Technology (IFOST), pp. 475-478.
741 Zhang, J., Zhang, Z., Zhu, W., Meng, X., 2020. Boosted photocatalytic degradation of
742 Rhodamine B pollutants with Z-scheme CdS/AgBr-rGO nanocomposite. Applied Surface
743 Science 502, 144275.
744